P3D-BRNS v1.0.0: A Three-dimensional, Multiphase, Multicomponent, Pore-scale Reactive Transport Modelling Package for Simulating Biogeochemical Processes in Subsurface Environments

Amir Golparvar[1], Matthias Kästner[2] and Martin Thullner[1]

[1] UFZ- Helmholtz Centre for Environmental Research, Department of Environmental Microbiology, Leipzig, Germany

[2] UFZ - Helmholtz Centre for Environmental Research, Department Environmental Biotechnology, Leipzig, Germany

Correspondence: Amir Golparvar (amir.golparvar@ufz.de)

Abstract

The porous microenvironment of soil offers various environmental functions which are governed by physical and reactive processes. Understanding reactive transport processes in porous media is essential for many natural systems (soils, aquifers, aquatic sediments or subsurface reservoirs) or technological processes (water treatment, or ceramic and fuel cell technologies). In particular, in the vadose zone of the terrestrial subsurface the spatially and temporally varying saturation of the aqueous and the gas phase leads to systems that involve complex flow and transport processes as well as reactive transformations of chemical compounds in the porous material. To describe these interacting processes and their dynamics at the pore scale requires a well-suited modelling framework accounting for the proper description of all relevant processes at a high spatial resolution. Here we present P3D-BRNS as a new open-source modelling toolbox harnessing the core libraries of OpenFOAM and coupled externally to the Biogeochemical Reaction Network Simulator (BRNS). The native OpenFOAM Volume of Fluid solver is extended to have an improved representation of the fluid-fluid interface. The solvers are further developed to couple the reaction module which can be tailored for a specific reactive transport simulation. P3D-RBNS is benchmarked against three different flow and reactive transport processes; 1) fluid-fluid configuration in a capillary corner, 2) mass transfer across the fluid-fluid interface and 3) microbial growth with a high degree of accuracy. Our model allows for simulation of the spatio-temporal distribution of all bio-chemical species in the porous structure (obtained from μ-CT images), for conditions that are commonly found in the laboratory and environmental systems. With our coupled computational model, we provide a reliable and efficient tool for simulating multiphase, reactive transport in porous media.

1 Introduction

33 Subsurface environments (soils, aquifers, aqueous sediments) are (typically) porous media host a

34 multitude of biogeochemical processes and interactions and provide different versatile ecosystem

35 functions (e.g. C sequestration, compound degradation, nutrient retention, provision of food, fibers and

36 fuel, habitat for organisms, water retention and purification, etc. (Baveye et al., 2016). These processes

37 are controlled by various biological (e.g., microbial abundance and activity), chemical (e.g., distribution

38 of dissolved and volatile species, mineral composition and surface properties of the solid matrix) and

39 physical (e.g., porous structure and permeability, water saturation) properties of the system. These

40 features create a complex web of interactions, the magnitude and effectiveness of which change

41 dynamically in space and time (Graham et al., 2014). Microbial communities, for example, and their

42 metabolic capacity are considered to be directly related to energy and matter fluxes (Thullner et al., 2007)

43 which are in turn, governed by pore arrangements and their connectivity. Along with other environmental

44 factors this can also modify various properties of the porous media (e.g. by biomass accumulation on pore

45 walls (Thullner, 2010), or mineral dissolution or precipitation (Meakin and Tartakovsky, 2009), which in

46 turn are altering the conditions for biogeochemical processes, too.

47 In soils (or more generally the vadose zone) the dynamically varying distribution of the aqueous and

48 gaseous phase leads to specifically complex and variable constraints for biogeochemical processes. In the

49 past, obtaining (bio)chemical and microbiological information at the pore level was neither economically

50 nor logistically a feasible option (Baveye et al., 2014). Also for the sake of applicability, traditionally,

51 researchers had more tendency to look for macroscale solutions to tackle environmental issues (White and

52 Brantley, 2003). The macroscale view (experimental, theoretical or a mixture of both) serves well the

53 purpose of practical applicability (White and Brantley, 2003), but for example, in the context of

54 microbially mediated degradation processes in the vadose zone, it fails to provide insights on the driving

55 mechanisms, as it overlooks important contributing factors, such as the tortuous porous

56 structure/pathways open to the transport of bio-chemical species, non-uniform distribution of water and

57 air phases as well as nonlinear relation of local biomass concentration and the bulk nutrient concentration.

58 Evidence at microscopic level has shown that biological activity and evolution are more locally organized

59 (Kuzyakov and Blagodatskaya, 2015) where macroscopic studies lead to loss of crucial information. This

60 has motivated the development of sophisticated physics-based models implementing all aspects of

61 hydrological, geochemical and biological processes involved in microbial growth and evolution.

62 Reactive Transport Models (RTMs) are a class of mathematical models that have been applied

63 extensively to study biogeochemical systems for about four decades (Parkhurst and Appelo,

64 1999;Thullner et al., 2005;Thullner and Regnier, 2019;Meile and Scheibe, 2019). There is a long list of

65 principal factors and mechanisms governing biogeochemical reactions at the pore scale. Numerically,

66 these processes can be defined and solved either by fully (global) implicit approaches or by separating

67 and solving different components once at a time. For the continuum scale a wide range of reactive

68 transport models exist which allow for the simulation of biogeochemical processes (Steefel et al., 2015b).

69 In turn, at the pore scale, models combining the simulation of flow, transport and reactive

70 (biogeochemical) processes are scarce, and existing model developments are often driven by specific

71 research questions and/or are subject to severe simplifications in the description of the pore space

72 (Golparvar et al., 2021). Integrated models explicitly capturing simultaneously the structural properties of

73 the soil at the microscale, the resulting multiphase flow and multispecies reactive transport are hardly

74 available (Tian and Wang, 2019).

75 Recently, new frontiers of pore-scale RTMs are emerging with the advances in computational power as

76 well as with huge improvements in imaging techniques (e.g. in static and dynamic scanning of porous

77 structure as well as fluids' distribution (Schlüter et al., 2019) or in detecting bacterial distributions in soil

78 using e.g., catalyzed reporter deposition with fluorescence in situ hybridization (CARD-FISH) technique

79 (Schmidt et al., 2015). Direct Numerical Models (DNMs) are becoming the nexus of next generation of

80 RTMs as they represent the porous structure in a fully explicit manner (directly obtained from soil

81 samples, digitized and fed into RTMs) in addition to offering a more flexible coupling of different

82 components of reactive transport models (Baveye et al., 2018;Raeini et al., 2012;Li et al., 2010;Yan et al.,

83 2016). Another advantage of using DNMs is that they offer a great deal of flexibility in considering

84 settings and conditions that are experimentally impossible to impose (Tian and Wang, 2019).

85 In this work, we introduce the pore-scale RTM package P3D-BRNS explicitly involving the structure and

86 topology of the pore space, the co-existence/co-flow of both the aqueous and the gaseous phase, the

87 advective-diffusive transport of species in each phase, and an arbitrary set of reactive processes controlled

88 by kinetic rate laws or thermodynamic constraints. The fluid flow field is updated via solving the Navier-

89 Stokes (NS) equation (Patankar and Spalding, 1972). The Volume-Of-Fluid (VOF) approach is adopted to

90 account for different phase distribution (Hirt and Nichols, 1981). The transport of chemical species is

91 considered via solving the Advection-Diffusion-Reaction Equation (ADRE), where the concentration

92 jump for soluble/volatile compounds across the fluid/fluid interface is modelled via the Continuous

93 Species Transfer (CST) method (Haroun et al., 2010). Reactive processes are defined and simulated

94 externally via coupling the flow and transport model to the BRNS (Biogeochemical Reactions Network

95 Solver) package (Regnier et al., 2002;Aguilera et al., 2005). The model structure is introduced and the

96 model performance is shown and compared with analytical counterparts. The model capabilities are

97 depicted for a fully three-dimensional case.

2 Mathematical Formulation

99 The entire numerical domain (Ω) can be decomposed to two main sub-regions: solid space (Ω_S) and void

100 space (Ω_ϑ). The void space is further divided into aqueous phase ($\Omega_{\vartheta,aq}$) and gaseous phase ($\Omega_{\vartheta,gs}$)

101 which are partitioned by the fluid-fluid interface (Ω_I). The overall domain is bounded externally between

102 inlet (Ω_{in}) and outlet (Ω_{out}) boundaries, which allow for inflow/outflow of different phases and chemical

103 species, as well as no-flux boundaries resembling physical walls, where nothing is allowed to leave or

104 enter the domain (Ω_{wall}). The domain is limited internally by no-flow boundaries where solid space and

105 void space intersect (i.e. solid surface, $\Omega_\vartheta \cap \Omega_S = \Omega_{wall}$).

2.1 Fluid Flow: Governing Equations

107 Evolution of a single/multi-phase, isothermal, incompressible, immiscible fluid(s) can be expressed by

108 basic conservation principles. These can be formulated into a single-field formalism (Hirt and Nichols,

109 1981):

$$\nabla \cdot \boldsymbol{u} = 0 \qquad in \; \Omega_\vartheta \tag{1}$$

$$\rho\left(\frac{\partial \boldsymbol{u}}{\partial t} + \boldsymbol{u} \cdot \nabla \boldsymbol{u}\right) = -\nabla P + \nabla \cdot \tau + \rho g + F_\sigma \qquad in \; \Omega_\vartheta \tag{2}$$

110 where $\boldsymbol{u}$ is the vector of velocity field, $\boldsymbol{\rho}$ is the fluid density, $\boldsymbol{P}$ is the pressure, $\boldsymbol{g}$ is the gravitational

111 vector, and $\boldsymbol{\tau}$ is the stress tensor which can be defined as $\tau = 2\mu S = 2\mu(0.5[(\nabla \boldsymbol{u}) + (\nabla \boldsymbol{u})^T])$ with $\boldsymbol{\mu}$ as

112 the fluid viscosity. $\boldsymbol{F_\sigma}$ denotes the interfacial tension force, which is nonzero only when two or more

113 phases (excluding solid) are available.

114 In case of simultaneous flow of two different phases (e.g. flow of air and water under unsaturated conditions

115 - Figure 1: Illustration of a porous medium at the microscale with one fluid invading the other (on the

116 left). Mathematical representation of the phase saturation in the computational cells around the interface

117 (on the right). The dashed line shows the actual location of the interface while values in each cells show

118 the amount of water saturation relevant to topology of the dashed line. Black dots represent volatile

119 compounds able to cross the fluid-fluid interface; green dots represent non-volatile compounds restricted

120 to the transport in the aqueous phase.), their locations and distribution are represented via introducing an

121 indicator function, $\boldsymbol{\alpha}$, taking values within the range $[0, 1]$. The first continuous fluid is marked as $\alpha = 1$,

122 the second fluid is denoted as $\beta = 1 - \alpha$ and for the transition from one fluid to the other (i.e. the interface,

123 Ω_I), α varies between 0 and 1. Fluid density and viscosity in each grid cell is then calculated from a linear

124 interpolation of this indicator function:

$$\rho = \alpha\rho_1 + (1-\alpha)\rho_2 \qquad in\ \Omega_\vartheta \tag{3}$$

$$\mu = \alpha\mu_1 + (1-\alpha)\mu_2 \qquad in\ \Omega_\vartheta \tag{4}$$

125   A mass conservative boundary condition at the fluid-fluid interface is written as:

$$\llbracket \rho_i(\boldsymbol{u}_i - w) \cdot n_{\Omega_I} \rrbracket = 0 \qquad in\ \Omega_I \tag{5}$$

126
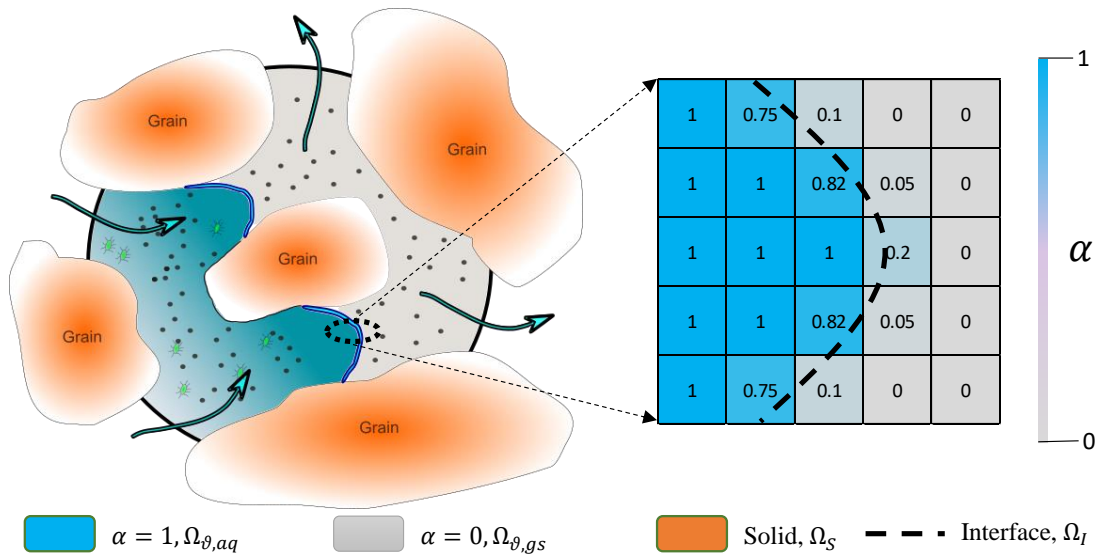
Figure 1: Illustration of a porous medium at the microscale with one fluid invading the other (on the left). Mathematical representation of the phase saturation in the computational cells around the interface (on the right). The dashed line shows the actual location of the interface while values in each cells show the amount of water saturation relevant to topology of the dashed line. Black dots represent volatile compounds able to cross the fluid-fluid interface; green dots represent non-volatile compounds restricted to the transport in the aqueous phase.

127   with ρ_i as the density of ith fluid, $\boldsymbol{u}_i$ as the velocity of ith fluid, w as the velocity of the interface, n_{Ω_I} as

128   the normal vector to the interface (Ω_I) pointing from the invading phase to the displaced one and the

129   brackets showing the jump condition at the interface.

130   In the context of the Finite Volume Method (FVM), discretization of the physical domain produces a

131   finite subset of discrete volumes (taking the shape of a polyhedral). The key implication of the Volume of

132   Fluid method is to define and solve for global variables, rather than having one equation for each variable

133   in each phase. Hence, the idea is to transform the integro-differential equations into their global versions

134   by averaging them over each cell volume (Whitaker, 2013). For multiphase systems, after a few steps of

135   linearization and approximation (see Hirt and Nichols (1981) for a detailed derivation), the Volume of

136   Fluid formulation of the momentum equation (2) is obtained as:

$$\rho\left(\frac{\partial \overline{\boldsymbol{u}}}{\partial t} + \overline{\boldsymbol{u}} \cdot \nabla \overline{\boldsymbol{u}}\right) = -\nabla P + \nabla \cdot \mu(\nabla \overline{\boldsymbol{u}} + (\nabla \overline{\boldsymbol{u}})^t) + \rho g + F_\sigma \qquad in \; \Omega_\vartheta \tag{6}$$

137 with having $\overline{\boldsymbol{u}}$ as the global averaged velocity vector. For the sake of simplicity, we drop the "average"

138 notation from the global velocity vector (i.e. will refer to $\overline{\boldsymbol{u}}$ as $\boldsymbol{u}$), for the rest of this paper.

139 A global, mass conservative, advection equation is used to describe the evolution of the indicator

140 function:

$$\frac{\partial \alpha}{\partial t} + \nabla \cdot (\alpha \boldsymbol{u}) + \nabla \cdot (\alpha(1-\alpha)\boldsymbol{u_c}) = 0 \qquad in \; \Omega_\vartheta \tag{7}$$

141 where α indicates the volume fraction of phase 1, $u_c = u_\alpha - u_\beta$ is the vector of the compressive velocity

142 with $u_{\alpha,\beta}$ as velocity vector of phase α and β right on the edge of the interface (detailed explanation on

143 deriving eq. (7) can be found in the Supplementary Information**Error! Reference source not found.**).

144 The latter term in equation (7) is active only in the presence of an interface. It is derived from mass

145 conservation equation written for phase α, which computationally helps with maintaining stiffness of the

146 interface. Since we don't solve for the velocity field of each phase individually, a direct calculation of u_c

147 is not possible. However, we can rather take an indirect approach for computing u_c as follows:

$$\boldsymbol{u_c} = min\left(c_\alpha |\boldsymbol{u}|, max(|\boldsymbol{u}|)\right)\frac{\nabla \alpha}{|\nabla \alpha|} \qquad in \; \Omega_I \tag{8}$$

148 In equation (8), c_α is a compression coefficient providing some level of control over how wide the

149 interface spans. A value of $c_\alpha = 0$ gives no compression of the interface, whereas values of $c_\alpha > 1$

150 provide an enhanced/sharper interface (Graveleau et al., 2017). In simulation scenarios introduced in this

151 paper, c_α has been assigned the value of 1, unless otherwise is stated.

152 To calculate the interfacial tension force, $\boldsymbol{F_\sigma}$, Brackbill et al., (1992) have introduced a Continuum

153 Surface Force (CSF) which requires computing the curvature of the interface:

$$\kappa = \nabla . n_{\Omega_I} \qquad in \; \Omega_I \tag{9}$$

154 with having κ as mean interface curvature, and n_{Ω_I} as the interface unit normal vector defined as:

$$n_{\Omega_I} = \frac{\nabla \alpha}{|\nabla \alpha|} \qquad in \; \Omega_I \tag{10}$$

155 Given the curvature, the interfacial tension force can be computed as:

$$F_\sigma = \sigma \kappa \nabla \alpha \qquad in \; \Omega_I \tag{11}$$

156 where σ is the surface tension between two fluids.

2.2 Reactive Transport: Governing Equations

157

158 Concentrations of mobile species are affected by advection (i.e. transport with the moving fluid),

159 molecular diffusion and reactive transformation. Also, in case of having two fluids simultaneously in the

160 system, different species can cross the fluid-fluid interface, causing local fluctuations in concentration

161 values. In general to account for all the changes in species concentrations, the ADRE for biogeochemical

162 reactive components can be written as:

$$\frac{\partial C_i}{\partial t} + \nabla \cdot (C_i \boldsymbol{u}) = -\nabla \cdot \left(J_{d,i} + J_{m,i} \right) + R_i \qquad in\ \Omega_\vartheta \tag{12}$$

163 where $J_{d,i}$ is the molecular diffusive flux of component i, $J_{m,i}$ is the mass flux of component i due to mass

164 transfer across the fluid-fluid interface and R_i accounts for the changes in concentration of component i

165 due to reactions. Molecular diffusion follows Fick's law:

$$J_{d,i} = -D_i \nabla(C_i) \qquad in\ \Omega_\vartheta \tag{13}$$

166 where D_i is the diffusion coefficient of species i. At the interface, the assumption of thermodynamic

167 equilibrium implies equality of chemical potentials. Given the condition that liquid concentration of

168 component i is proportional to the partial pressure of the species in the secondary phase (e.g. gas, oil or

169 minerals), a partitioning relationship such as Raoult or Henry's law (Danckwerts and Lannus, 1970) can

170 be established to relate species concentrations on both sides of the interface:

$$C_{i,\beta} = H_i C_{i,\alpha} \qquad in\ \Omega_I \tag{14}$$

171 with $C_{i,\alpha}$ as concentration of species i in phase α, H_i as Henry's constant of species i and $C_{i,\beta}$ as

172 concentration of species i in phase β. Depending on if a given compound's concentration in the aqueous

173 phase or the gaseous phase is multiplied by the Henry's coefficient, (14), the definition of Henry's

174 constant switches between the solubility or volatility for that compound (i.e. $H_i^{soluility} = {1}/{H_i^{volatility}}$)

175 (Sander, 2015). Unless otherwise stated, the volatility concept of Henry's law is adopted in order to

176 define the concentration relationship of a given compound across the fluid-fluid interface (14). The

177 concentration field around the fluid-fluid interface (where $\nabla \alpha \neq 0$) at equilibrium, for any values of $H \neq$

178 1, is discontinuous which imposes the additional flux, $J_{m,i}$, to satisfy the concentration jump across the

179 interface. Hence the mass transfer flux, $J_{m,i}$, can be derived within the VOF framework (i.e. CST) as

180 follows (Haroun et al., 2010):

$$J_{m,i} = -D_i \frac{1 - H_i}{\alpha + (1-\alpha)H_i} C_i \nabla \alpha \qquad in\ \Omega_\vartheta \tag{15}$$

181 It is noteworthy that few assumptions and volume averaging methods are implemented to derive equation

182 (15), which readers are encouraged to check the references for more details. The diffusion coefficient is

183 calculated from harmonic interpolation:

$$D_i = \frac{1}{\frac{\alpha}{D_{i,A}} + \frac{1-\alpha}{D_{i,B}}} \qquad in\ \Omega_\vartheta \tag{16}$$

184 where $D_{i,\alpha-\beta}$ is the diffusion coefficient of species i in phase α and β respectively.

185 Simulated reactions include kinetically as well as thermodynamically constrained reactions. For a

186 kinetically constrained reaction j the reaction rate $r_j = f(C_1, ..., C_n)$ is needed while for a

187 thermodynamically constrained reaction k the equilibrium conditions defined by a law of mass action

188 $M_k = f(C_1, ..., C_n)$ is needed with M_k as equilibrium constant. These equations can be of arbitrary form and

189 the resulting reaction network defines the term R_i in equation (12) (Aguilera et al., 2005;Regnier et al.,

190 2002). For immobile species concentration changes are only due to reactive processes.

2.3 Boundary Conditions (BCs)

192 There are various types of boundary conditions, corresponding the real physical conditions, most of which

193 can be derived from two basic types:

194 • Dirichlet boundary (fixed value) which relates the value of a variable at a given geometric

195 location to a constant value; e.g. $\boldsymbol{C_i} = 1M$ in Ω_{in} meaning a constant 1 molar concentration of

196 component $\boldsymbol{i}$ at the boundary,

197 • von Neumann boundary (fixed gradient) which provides the value of a variable's gradient at the

198 face of the boundary cell; e.g. $\partial_n \boldsymbol{p} = 0$ in Ω_{wall} giving a zero pressure gradient on the wall.

199 In general, our model can apply any of these basic boundary conditions to any scalar or vector variables

200 such as pressure, velocity/flux, concentration of volume of fluid fields, but one needs to assure that the

201 imposed BC(s) are both compatible and they reflect the correct physical boundary conditions. For

202 example, for velocity/flux-pressure coupling, a Dirichlet (i.e. constant) boundary for flux at the inlet can

203 be coupled with either 1) fixed discharge velocity/flux and zero gradient (i.e. von Neumann) pressure at

204 both inlet and outlet, or 2) a constant pressure head at the inlet and atmospheric pressure at the outlet with

205 zero gradient velocity/flux at both ends, or 3) fixed values of pressure and velocity/flux at one end and

206 zero gradient at the other end. In the beginning of section 2, typical composition and configuration of an

207 arbitrary computational domain is described. Inlet, outlet and impermeable boundaries are amongst the

208 most common types that one might face. Inlet BC means for the direction of fluid flux to be pointing

209 inwards (i.e. into the domain) while for the outlet, the direction of the flux should be outwards. Also for

210 the impermeable wall, zero-orthogonal fluxes need to be satisfied. Either Dirichlet, von Neumann or a

211 mixture of both can be used at a particular boundary. Mathematical translation and implementation of

212 these boundaries are provided in the next section. Time-dependent BCs (e.g. cyclic or seasonal

213 water/species influx) are also readily available to be applied, but never been used in this work. Unless

214 otherwise stated, boundary conditions that have been imposed on each section of the computational

215 domain are described as follows:

216 **At impermeable boundaries** (Ω_{wall}): Physical wall implies no flux perpendicular to the normal vector

217 to its surface. No slip BC is an appropriate BC for the velocity field on the wall. In general, they all can

218 be written as:

$$\partial_n \boldsymbol{C_i} = 0, \qquad \boldsymbol{u_{x,y,z}} = 0, \qquad \partial_n \boldsymbol{p} = 0, \qquad \partial_n \boldsymbol{\alpha} = 0 \qquad in \ \Omega_{wall} \tag{17}$$

219 For the velocity field, on the wall, a slip boundary condition is also available to be applied.

220 **At inlet/outlet boundaries** ($\Omega_{in}, \Omega_{out}$): Concentration of reactants, products and inert tracers are set to

221 fixed values at inlet, while they are allowed to leave the domain at outlet with zero gradient boundary

222 condition. Constant flowrate with zero pressure gradient is applied at inlet and an atmospheric pressure

223 (fixed value) with zero velocity gradient is set at outlet. Also in case of two-phase flow, the invading

224 phase is set to enter from inlet at fixed value and exits from outlet with zero gradient BC. Mathematically,

225 they can be expressed as:

$$C_i \geq 0, \qquad \boldsymbol{u} = const., \qquad \partial_n \boldsymbol{p} = 0, \qquad \alpha = const. \qquad in \ \Omega_{in} \tag{18}$$

226 together with:

$$\partial_n \boldsymbol{C_i} = 0, \qquad \partial_n \boldsymbol{u_n} = 0, \qquad \boldsymbol{p} = 0, \qquad \partial_n \boldsymbol{\alpha} = 0 \qquad in \ \Omega_{out} \tag{19}$$

227 While we have mostly applied equations (18) and (19) for designing an inlet/outlet duo, other formats,

228 such as defining a pressure head (plus zero gradient velocity) on the inlet in combination with either

229 constant exit pressure or constant discharge rate, are readily available to implement as well.

230 **At the fluid-fluid-solid contact line** (Ω_{l^3})**:** At the fluid-fluid-solid contact line, in case of no interactions

231 or no reaction of any chemical species with the solid, the boundary condition at the triple point is derived

232 to be:

$$\nabla C_i \cdot \boldsymbol{n_s} = \frac{H_i - 1}{\alpha H_i + (1 - \alpha)} C_i \nabla \alpha \cdot \boldsymbol{n_s} \qquad in \ \Omega_I \tag{20}$$

233 with $\boldsymbol{n_s}$ as the normal vector to the solid surface (Graveleau et al., 2017). Also, the concept of contact

234 angle is applied by making the following modification to the interface normal vector:

$$\mathrm{n}_{\Omega_{l^3}} = cos\theta \boldsymbol{n_s} + sin\theta \boldsymbol{t_s} \qquad in\ \Omega_{l^3} \tag{21}$$

235 where $\boldsymbol{n_s}$ is normal vector and $\boldsymbol{t_s}$ is the tangential vector to the solid surface (Brackbill et al., 1992). CSF,

236 though, has been reportedly generating non-physical spurious currents (Scardovelli and Zaleski, 1999).

237 For this, many have tried to eliminate/mitigate this issue by explicit representation of the interface either

238 via using the Geometric VOF method (Popinet, 2009) or coupled Level-set (LS) VOF functions

239 (Albadawi et al., 2013). Geometric VOF is quite suitable for structured grids, but for porous structures

240 with highly unstructured grids, the calculations can become quite complicated. Alternatively, Raeini et al.

241 (2012) suggested filtering the capillary forces parallel to the interface, which can significantly reduce the

242 non-physical velocities. In short, the modifications they proposed and which are used here are: 1)

243 smoothing the indicator function to have a better measure of the interface curvature, 2) sharpening the

244 indicator function for computation of the interfacial tension force, 3) filtering the capillary pressure force

245 parallel to the interface, and 4) filtering capillary fluxes based on the capillary pressure gradient.

2.4   Numerical Formulation

247 The mass conservation (eq. (1), momentum (NS - eq. (2) and indicator function (eq. (7) equations are all

248 implemented within the open source computational fluid dynamics (CFD) package, OpenFOAM

249 (Greenshields, 2015). OpenFOAM utilizes the finite volume methodology (FVM), a common choice for

250 CFD problems as FVM works only with conservative flux evaluation at each computational cell's

251 boundaries, making it robust in handling nonlinear transport problems. Also all the differential equations

252 mentioned before are first written in their integral form over each cell volume and then converted to the

253 surface summations using Green's Theorem.

254 In this work, the original two-phase (VOF) flow solver, i.e. *interFoam*, is modified to construct our

255 biogeochemical reactive transport package. The momentum equation (2) is linearized in a semi-discrete

256 form as:

$$A_d \boldsymbol{u} = \boldsymbol{H}(\boldsymbol{u}) - \nabla P + \boldsymbol{F}, \tag{22}$$

257 where A_d holds the diagonal elements of the coefficient matrix, $\boldsymbol{H}(\boldsymbol{u})$ contains off-diagonal elements of

258 the coefficient matrix including all source terms, and $\boldsymbol{F}$ entails any body forces (interfacial tension force

259 only in this case). Temporal discretization is handled via the first order Euler method while spatial

260 discretization is managed via second order finite volume schemes. Convection terms of the momentum

261 equation and indicator function (7) are computed using a bounded self-filtered central differencing

262 (SFCD) scheme (based on Gauss's theorem). Rearranging equation (22) for velocity and imposing the

263 continuity equation (1), the following linear pressure equation can be obtained:

$$\sum_f \frac{S_f}{\langle A_d \rangle_f} \nabla_f^\perp P = \sum_f \left(\langle \frac{\boldsymbol{H(u)}}{A_d} \rangle_f \cdot |S_f| + \frac{\varphi_{F,f}}{\langle A_d \rangle_f} \right). \tag{23}$$

264 S_f in equation (23) denotes the outward area-vector of face f, the notation $\nabla_f^\perp$ shows face normal

265 gradients calculated right on the face centers, $\langle \rangle_f$ shows the interpolated values of a face-centered

266 parameter from its cell-centered counterpart, and $\varphi_{F,f}$ is the interfacial force flux term.

267 The velocity-pressure coupling of equations (1) and (2) are solved using Pressure Implicit with Splitting

268 of Operators (PISO) (Issa, 1986). PISO embodies a predictor-corrector strategy to simultaneously update

269 pressure and velocity within each time step. The resultant system of equations are solved on the cell faces

270 and then interpolated back to calculate velocities and pressure at the cell centers. The coupling of

271 indicator function (eq. (7)) and momentum equation is explicitly defined and solved right after the PISO

272 step is finished. Within the same time step, transport and reaction of different species are then solved

273 sequentially – using a Sequential Non-Iterative Algorithm (Steefel et al., 2015a;Steefel and MacQuarrie,

274 1996). Time step size is controlled by introducing a Courant number. Time is discretized using either

275 Euler or Crank-Nicholson methods and spatial discretization is performed using the Van Leer second

276 order Total Variation Diminishing scheme (TVD) (van Leer, 1979).

277 The reaction network is built separately and externally solved within the BRNS package - which employs

278 first order Taylor series expansion terms and uses Newton-Raphson method to iteratively solve the

279 system of linear equations (Regnier et al., 2002). BRNS utilizes MAPLE programming language to

280 construct the Jacobian matrix (which contains the partial derivatives of unknown parameters, i.e.

281 concentrations) and other problem-related data such as rate parameters and translating them to a

282 FORTRAN package. The FORTRAN code is then compiled to generate shared object (*.so file) that can

283 be dynamically called later from the transport solver (Centler et al., 2010). The significance of having

284 dynamically shared object file is more apparent when running computationally-demanding

285 cases/scenarios while decomposing and running the application in parallel. BRNS is invoked once the

286 new concentrations are computed from the transport solver. The updated concentrations from the BRNS

287 library (i.e. updating concentrations from redox reactions) are then fed back into the transport solver

288 before moving to the next time step. This process repeats until the final time is reached. This coupling

289 scheme has been successfully used for other RTM approaches before (Centler et al., 2010;Gharasoo et al.,

290 2012;Nick et al., 2013).

291 Prior to run simulations, the physical settings of the domain are required to be specified; i.e. the physical

292 geometry of the pore space with proper boundaries and the meshing scheme should be designed.

293 OpenFOAM provides a basic utility for defining boundaries as well as mesh generation which are

294 translatable by the OpenFOAM engine. Any other meshing software/freeware can be freely used as long

295 as an OpenFOAM-compatible format for the meshed file can be created. The overall workflow required

296 to build and run a case/scenario is summarized in Figure 2.
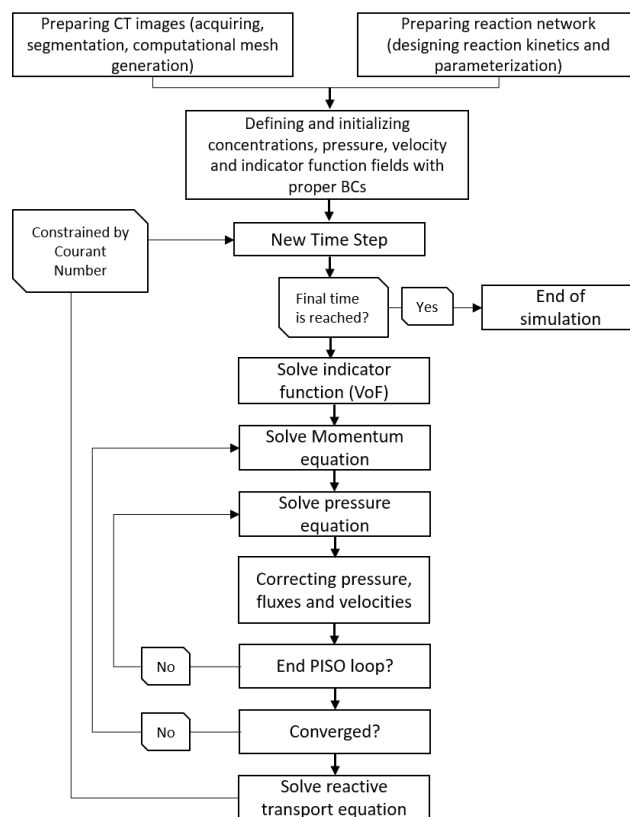
297

298 **Figure 2**: Full solution procedure to simulate a reactive transport process at its fullest complexity.

3 Model Performance

300 The presented reactive transport model is designed 1) to capture real world pore structures in up to three

301 dimensions, 2) to explicitly simulate the transient distribution of a gas and a liquid phase within the entire

302 pore space and 3) to simulate a full set of advection-diffusion-reaction mechanisms. To validate different

303 features of the model various simplified scenarios were used which allow the use of analytical

304 expressions as reference for the numerical results. We here show three representative test scenarios

305 addressing different features of the model (two-phase flow, mass transfer across the fluid-fluid interface

306 and reactive transport) individually. Subsequently, the model capabilities are depicted in a final

307 biodegradation scenario making use of the various model features simultaneously.

308   3.1   Fluid Configurations

309   In order to test our model's performance in simulating two-phase flow, we have zoomed into a two-

310   dimensional porous structure and isolated only one single corner taking the shape of an equilateral

311   triangle. Initially, two immiscible fluids (one wetting, and one non-wetting, e.g. water and air) are placed

312   in such a way that their interface forms a straight line (Figure 3, a). The side length of the triangle is 1 mm

313   with a mesh size of 1 μm. Under thermodynamic equilibrium conditions, the force exerted by the pressure

314   difference between two phases is countered by the interfacial tension force. This, along with the contact

315   angle of the non-wetting phase at the wall surface in presence of the wetting phase (e.g. water),

316   determines the topology of the fluid-fluid interface. For a given corner half-angle, the distance that

317   wetting phase spreads over the solid surface from the corner vertices (the highlighted section with green

318   color on Figure 3, b), b, can be calculated as:

$$b = r \frac{\cos(\theta + \beta)}{\sin(\beta)} \tag{24}$$

319   with r as the radius of the interface's curvature, θ as the contact angle and β as the corner half-angle

320   (Blunt, 2017). In order to reach thermodynamic equilibrium, we performed transient, two-phase flow

321   simulations to compute velocity, pressure and indicator function fields until the triple contact line (Ω_{l^3}) is

322   static. For this, we first divided the equilateral triangle in half, as the problem is symmetrical along the

323   height of the triangle. The symmetrical plane implies that there is no gradient (of any scalar or vector

324   field) perpendicular to its surface while the tangential components (of all fields) remain the same. To find

325   the fluid configuration at equilibrium, we simulated the two-phase flow scenario in two steps. First, we

326   applied a closed boundary condition on the bottom domain by setting $\boldsymbol{u} = 0$ together with $\partial_n p = 0$. Also

327   a closed boundary is imposed on the topmost part of the domain which follows the same BC as the

328   bottom. This way, the interface is able to reconfigure and reorient itself in order to recreate the imposed

329   contact angle with the wall, and at the same time, pressure is allowed to build up in both phases to support

330   the shape of the interface. Then, in order to obtain an equilibrium curvature for the interface, bottom and

331   top domains are opened. This is achieved by setting the 1) pressure in Ω_{in} to the average pressure within

332   the non-wetting phase, 2) pressure in Ω_{out} to the average pressure within wetting phase together with 3)

333   $\partial_n \boldsymbol{u} = 0$ on both Ω_{in} and Ω_{out}. At this stage, we applied a special BC for the indicator function to allow

334   the fluids to enter or leave the domain at both ends, so that the interface can freely transition to its static

335   shape. At the inlet (Ω_{in}), the BC for α is set to switch between $\partial_n \boldsymbol{\alpha} = 0$, if the fluid flux is pointing

336   outwards, and $\boldsymbol{\alpha} = 0$ if the fluid flux is directed into the domain. Also at the outlet (Ω_{out}), the BC for α

337   switches between $\boldsymbol{\alpha} = 1$, if the fluid flux is inwards, and $\partial_n \boldsymbol{\alpha} = 0$, if the fluid flux is outwards. This

338   ensured that appropriate fluids entered the domain from either inlet or outlet boundaries. The radius of

339   curvature can be also evaluated from the Young-Laplace equation ($P_c = \frac{\sigma}{r}$). With a pressure difference of

340   255.33 (kg m^{-1} s^{-2}) obtained from the last step and a surface tension of 0.07 (kg s^{-2}), the radius of

341   curvature is calculated to be 2.17e-4 m. In a different approach, once the interface attains stationarity, we

342   calculated r for equation (24) as the reciprocal of the interface's mean curvature (2.77e-4 m). For a

343   contact angle of 10° and a corner half-angle of 30°, the analytically calculated value for the length, b, of

344   the section in contact with the wetting phase is 375 µm, while the numerical solution yields 370 µm.

345   With a relative error of 1.21% this shows a reasonable match between numerical and analytical solutions

346   in modelling two-phase flow.

347
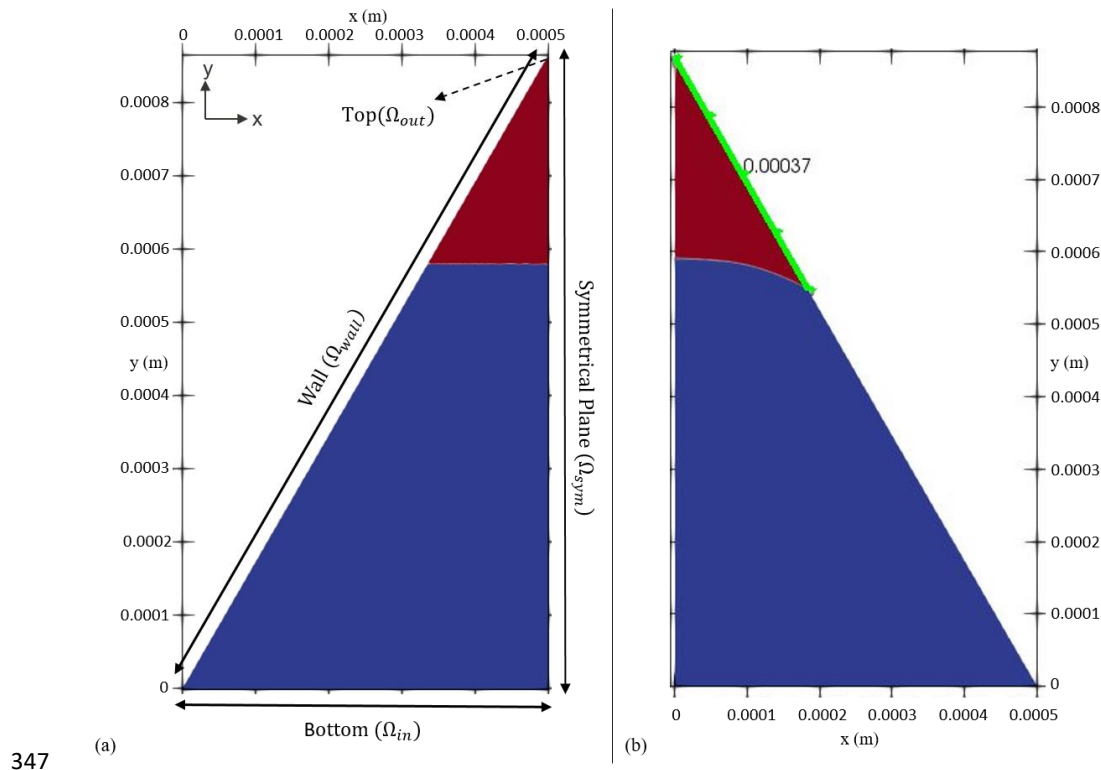
348   **Figure 3**: Initial condition (a) versus final arrangement (b) of the two phases in the fluid configurations scenario. The blue color
349   indicates the non-wetting and the red color shows the wetting phases respectively. The dashed arrow shows the location of the
350   outlet, while the solid-line arrows depict the extent of others boundaries. Once equilibrium is reached (figure b), the curvature of
351   the interface corresponds to the force balance between pressure difference across the interface and the surface tension which can
352   be used to verify the model's sanity. The distance of the contact point (i.e. the point/line where all three phases – water, air and
353   solid – meets) from the corner vertex (highlighted as green), also provides another measure for checking the accuracy of the
354   numerical model.

355   3.2   Mass Transfer across the Fluid-Fluid Interface

356   Mass transfer of dissolved species between different phases, is particularly of importance for various

357   biogeochemical processes in unsaturated subsurface environment as e.g., oxygen or volatile organic

358   carbon compounds are found in the liquid and the gas phase, yet their transport and reaction conditions

359   differ highly between these two phase

360   Model performance in simulating mass flux across the fluid-fluid interface is validated via a numerical

361   experiment in which two immiscible stationary fluids (an aqueous - α - and a gaseous - β - phase, $\mathbf{u} = 0$ in

362   Ω_{ϑ}) are horizontally (to remove buoyancy effects) residing on a one dimensional tube of 10 mm length

363   with mesh size of 100 µm. The general partial differential equation (PDE) of equation (12) takes the form

364   of a simple diffusive transport as:

$$\frac{\partial C_{tr,i}}{\partial t} - D_{tr,i} \nabla(C_{tr,i}) = 0 \qquad i = aq, gs$$

$$BC - 1: \quad C_{tr,aq} \times H = C_{tr,gs} \qquad in \ \Omega_I \tag{25}$$

$$BC - 2: \quad D_{tr,aq} \frac{\partial C_{tr,aq}}{\partial x} = D_{tr,gas} \frac{\partial C_{tr,gs}}{\partial x} \qquad in \ \Omega_I$$

365   with C_{tr} as the concentration of a volatile tracer and $D_{tr,i}$ as the diffusivity of the tracer in phase i. Each

366   phase is set to occupy half of the total volume (Figure 4-a). The system is initialized with a volatile

367   chemical species of concentration of 1 mol m⁻³ in $\Omega_{\vartheta,aq}$, and 0 mol m⁻³ in $\Omega_{\vartheta,gs}$. At the inlet and the outlet

368   boundary, tracer concentration equals that of the nearest solution such that, in short simulation time, it

369   yields no concentration gradient into or out of the domain. The tendency of the dissolved chemical

370   component to cross the fluid-fluid interface is expressed using a constant Henry coefficient. Tracer

371   diffusivity is set to be 1e-5 m² s⁻¹ in both phases. The analytical solution for equation (25) can be found in

372   Bird (Bird, 2002).

373   Three scenarios with low, neutral, and high affinity of the volatile compound towards the gaseous phase

374   are considered with corresponding Henry coefficients of 0.01 (low volatility, similar to naphthalene), 1

375   (moderate volatility, e.g., vinyl chloride) and 100 respectively (high volatility, e.g. heptane). For a low

376   value of H ($H = 0.01$ – Figure 4-b) little (almost no) tracer is crossing the interface, while at neutral

377   condition ($H = 1$ – Figure 4-c), tracer diffusion is invariant to the phase it is occupying. Evidently for

378   high values of H ($H = 100$ – Figure 4-d), strong depletion of the tracer in aqueous phase as well as the

379   concentration jump across the interface are observed. The numerical results are ubiquitously identical to

380   the results of the analytical solution (Figure 4-b, c, d).

381
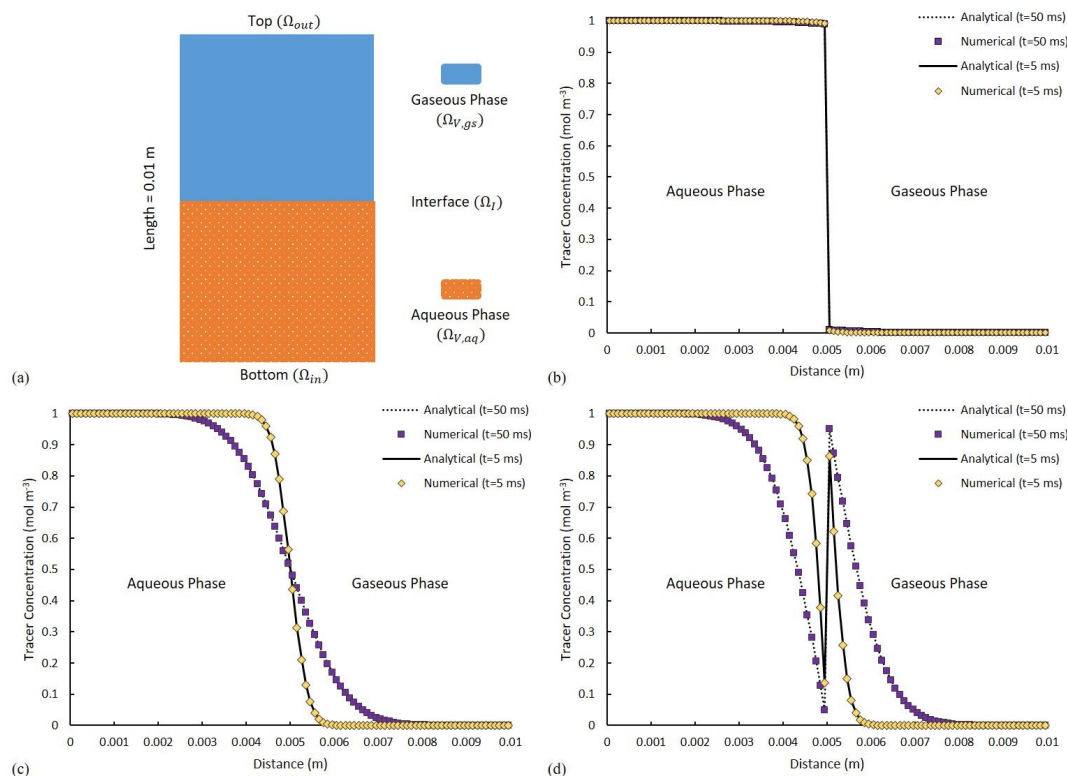
Figure 4: (a) A schematic of the fluid distributions at initial condition. The solid and dotted lines show the analytical solutions with purple and yellow squares depicting the numerical solutions. Comparison of the analytical and numerical solutions of tracer distribution at two distinct time points of t_1=5ms and t_2=50ms for (b) H = 0.01, (c) H = 1, and (d) H = 100.

3.3 Microbial Growth and Reactive Transport

Our modelling framework can parameterize any type of reactions, we put the main focus in this subsection on microbially driven redox transformations (i.e. a type of reactions commonly encountered in soils and other porous media environments) and on the implementation of the corresponding mathematical formulation. To validate our model with a scenario in which bacterial biomass is allowed to evolve (i.e. to grow and to decay) we adapted a conceptual biodegradation scenario from Cirpka and Valocchi (2007b) in which a fully-water-saturated, two-dimensional domain is subjected to a constant flux of two different components; ED (electron donor – e.g. hydrocarbon) and EA (electron acceptor – e.g. oxygen). The bacteria residing in the channel, facilitate the reaction between ED and EA, which can be written in an abstract form as $f_a ED + f_b EA \xrightarrow{biomass} f_c Prod$, where $biomass$ is the microbial biomass, $Prod$ is the product(s) (e.g. metabolites such as carbon dioxide) and f_a, f_b and f_c are

stochiometric coefficients. Assuming a double-Monod kinetics for expressing microbial growth and the
microbially driven reaction rates, as well as assuming none of the reactants nor products are involved in
secondary reactions, the ADRE (eq. (12)) for each chemical species can then be written as:

$$\frac{\partial C_{ED}}{\partial t} + \boldsymbol{u}\frac{\partial C_{ED}}{\partial x} - D_t\frac{\partial^2 C_{ED}}{\partial y^2} = -\frac{C_{ED}}{C_{ED} + K_{ED}}\frac{C_{EA}}{C_{EA} + K_{EA}}\frac{\mu_{max}}{Y}f_a C_{bio} \qquad in\ \Omega_\vartheta$$

$$\frac{\partial C_{EA}}{\partial t} + \boldsymbol{u}\frac{\partial C_{EA}}{\partial x} - D_t\frac{\partial^2 C_{EA}}{\partial y^2} = -\frac{C_{ED}}{C_{ED} + K_{ED}}\frac{C_{EA}}{C_{EA} + K_{EA}}\frac{\mu_{max}}{Y}f_b C_{bio} \qquad in\ \Omega_\vartheta$$

$$\frac{\partial C_{Prod}}{\partial t} + \boldsymbol{u}\frac{\partial C_{Prod}}{\partial x} - D_t\frac{\partial^2 C_{Prod}}{\partial y^2} = \frac{C_{ED}}{C_{ED} + K_{ED}}\frac{C_{EA}}{C_{EA} + K_{EA}}\frac{\mu_{max}}{Y}f_c C_{bio} \qquad in\ \Omega_\vartheta \qquad (26)$$

$$\frac{\partial C_{bio}}{\partial t} = \frac{C_{ED}}{C_{ED} + K_{ED}}\frac{C_{EA}}{C_{EA} + K_{EA}}\mu_{max} C_{bio} - \lambda C_{bio} \qquad in\ \Omega_\vartheta$$

where $\boldsymbol{u}$ is the velocity (which has only a constant x-component), D_t is the transverse dispersivity,
C_{ED}, C_{EA}, C_{Met} and C_{bio} are concentrations of $ED, EA, Prod$ and $biomass$ respectively; K_{ED} and K_{EA} are
half saturation constants for respective compounds in the biomass growth term, Y is the yield coefficient,
μ_{max} is the maximum bacterial growth rate, and λ is the bacterial decay rate. Using these equations
Cirpka and Valocchi (2007a) developed an analytical solution for steady-state conditions, which in the
version of Cirpka and Valocchi (2009) is used as reference for the numerical results.

The numerical experiment is designed to have ED and EA, occupying 25% and 75% of the inlet
repectively, and, simultaneously, invading the domain under a constant uniform velocity field, with
concentration of C_{ED}^{inlet} and C_{EA}^{inlet}. In a real-world scenario, this can be seen as a plume of a contaminant
(i.e. a hydrocarbon as ED) being carried into the domain within an oxygenated stream and essentially we
are interested in knowing the final concentration/distribution of all bio-chemical species within the
domain. The parameters used in this scenario are summerized in Table 1. Transient reactive transport
simluations are perfomed until a steady state is achieved. For validation, we analyze all concentration
profiles along the y-axis at a fixed distance of $\boldsymbol{x}$ =2 m and compare them with the analytical solutions.
The analytical and numerical results show an almost perfect agreement (Figure 5, b-e).
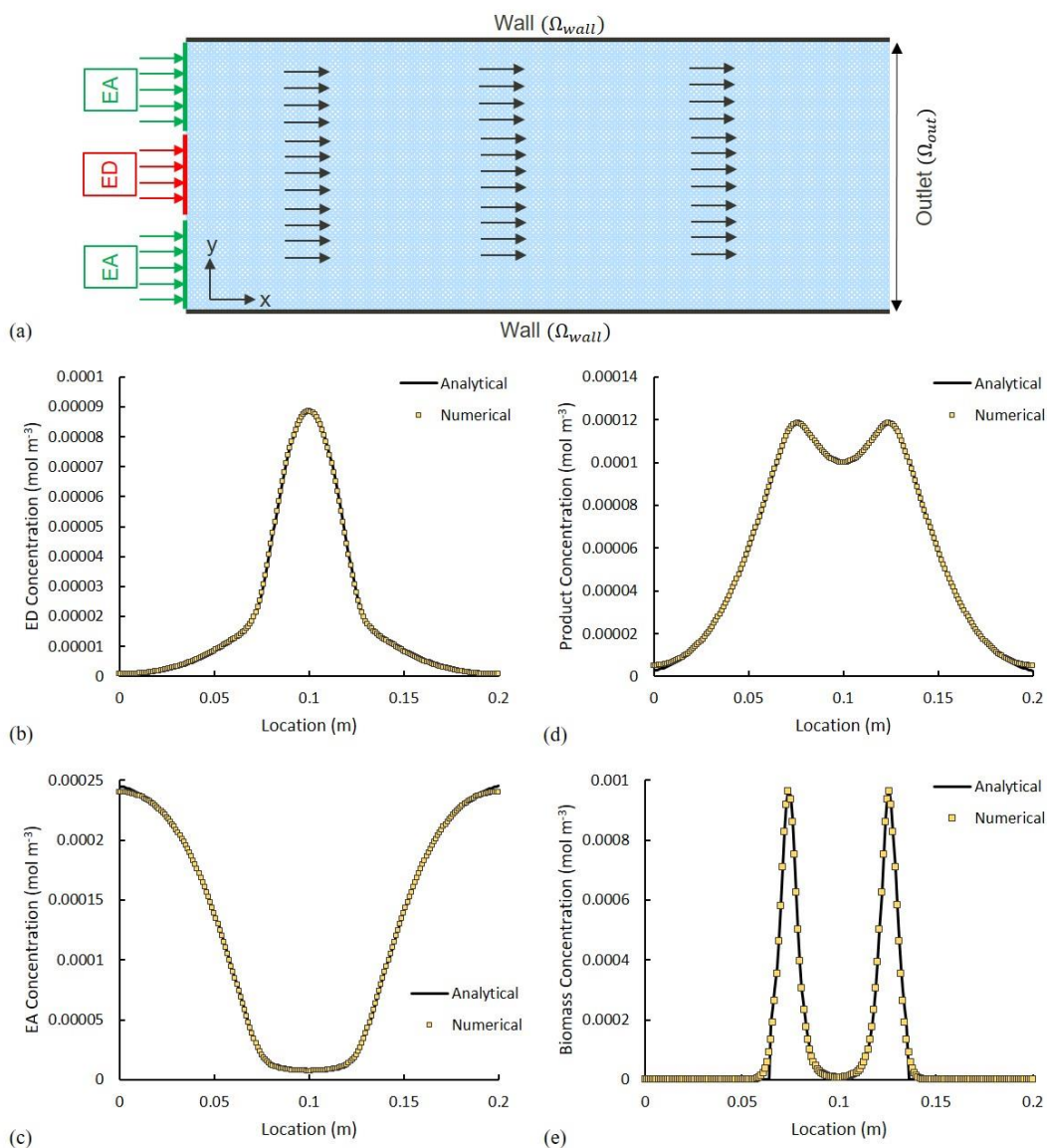
Figure 5: (a) Model set up. The arrows show the direction of the flow field. Solid lines show the analytical solution and the yellow squares illustrate the numerical results. (b-e) Comparison of the analytical and numerical solutions x=2m for concentration of (b) *Electron Donor*, (c) *Electron Acceptor*, (d) *Product*, and (e) *Biomass*.

421   Table 1: Parameter values used for simulating microbial growth.

Parameter	Value	Unit	Parameter	Value	Unit
$\boldsymbol{u}$	100	$cm\ d^{-1}$	μ_{max}	1	d^{-1}
Domain width	20	cm	Domain length	500	cm
D_t	2.5	$cm^2\ d^{-1}$	λ	0.1	d^{-1}
f_a, f_b, f_c	1	-	K_{ED}	8.33e-2	mM
C_{ED}^{inlet}	0.33	mM	K_{EA}	3.13e-2	mM
C_{EA}^{inlet}	0.25	mM	Y	1	–
Mesh size	0.2	mm			

422

3.4   Theme: Demonstrating Model Capabilities

424 The scenarios described above are designed to serve as the sole purpose of creating a baseline for

425 validating the numerical toolbox – simple enough where analytical solutions could exist. Unlike the

426 simplicity introduced in previous sections, simulating soil processes with all of the complexities, though,

427 would require having all the modelling elements to be present. We thus present here a scenario with an

428 unsaturated soil hosting the facultative anaerobic bacteria *Agrobacterium tumefaciens*, which performs

429 aerobic respiration under oxic condition, but switches to denitrification using nitrate, nitrite or nitric oxide

430 under anoxic condition (Kampschreur et al., 2012). This example allows us to show our model

431 capabilities, as it involves 1) the actual micro structure of the soil, 2) unsaturated conditions, and 3) an

432 enzymatic reaction network with limiting/inhibition terms. The microstructure is obtained via

433 subsampling from a larger µ-CT image with voxel size of 6 micron (see Supplementary Information). A

434 two-phase simulation is then performed on the voxelized subsample to obtain the fluxes and phase

435 distribution of air and water within the pore space. For this, the entire domain is initially filled with water

436 and subject to injecting air from the top boundary with constant flux of 0.013 ml h^{-1}. An important note to

437 make here is with a relatively high influx, advection transport acts as the bottleneck for numerical time

438 steps. Hence, reactions are performed at a quite slower pace (i.e. larger time steps). This separation of

439 processes helps improve the overall run-time of the simulations. Fluids are allowed to leave the domain

440 from the bottom part (kept at atmospheric pressure) while all the remaining sides are set to be

441 impermeable walls. Once fluid configurations in the domain are stationary, their distribution along with

442 the velocity profile are used as basis for the reactive transport simulations (phase distributions can be

443 found in the Supplementary Information). Using succinate ($C_4H_4O_4^{2-}$) as organic carbon substrate to be

444 degraded, a metabolic reaction network is constructed with four microbial degradation pathways each

445   following Monod-type kinetics: 1) aerobic respiration with a nitric oxide (*NO*) inhibitory term, 2) nitrate

446   (*NO₃⁻*) reduction, 3) nitrite (*NO₂⁻*) reduction and 4) *NO* reduction, with having oxygen (*O₂*) as inhibitory

447   element for all denitrification conversions (eq. (27). Also three additional equations are considered for the

448   synthesis of the three different enzymes required for degradation processes (eq. (28). We consider only

449   one single strain of bacteria (*Agrobacterium tumefaciens*) which has the benefits of performing both

450   aerobic respiration and denitrification. Bacteria are considered to be non-motile with an initial

451   concentration of 0.25 mol m^{-2} and uniformly covering the entire grain surface area. Succinate has its

452   initial concentration in the aqueous phase set at 0.2 *mM* (0 *mM* in the gaseous phase), while all other

453   species have their initial concentrations of 0 *mM* in both aqueous and gaseous phases. Boundary condition

454   for all concentration fields on all boundaries is set to zero gradient except for the inlet boundary (fully

455   saturated with air) - where for oxygen it is set to 0.03567 *mM*, and for all others is set to 0 *mM*. In order to

456   avoid depletion of the nitrate in the system, a nitrate concentration of 0.1 μM (as initial condition) is

457   provided. The complete reaction network can be written as follows (Kampschreur et al., 2012):

$$a)\ C_4H_4O_4^{2-} + 1.2O_2 + 1.56H^+ + 0.44NH_4^+ \rightarrow 2.2CH_{1.8}O_{0.5}N_{0.2} + 1.8CO_2 + 1.68H_2O$$

$$b)\ C_4H_4O_4^{2-} + 3.23NO_3^- + 1.6H^+ + 0.36NH_4^+$$
$$\rightarrow 1.8CH_{1.8}O_{0.5}N_{0.2} + 3.23NO_2^- + 2.2CO_2 + 1.92H_2O$$

$$c)\ C_4H_4O_4^{2-} + 6.45NO_2^- + 8.09H^+ + 0.36NH_4^+ \tag{27}$$
$$\rightarrow 1.8CH_{1.8}O_{0.5}N_{0.2} + 6.45NO + 2.2CO_2 + 5.15H_2O$$

$$d)\ C_4H_4O_4^{2-} + 6.45NO + 1.64H^+ + 0.36NH_4^+$$
$$\rightarrow 1.8CH_{1.8}O_{0.5}N_{0.2} + 3.23N_2O + 2.2CO_2 + 1.92H_2O$$
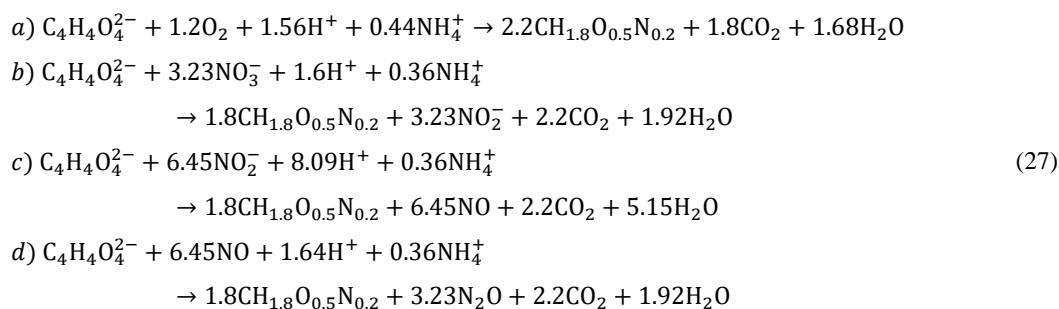
458   Several assumptions are made for preparing the kinetics of the reactions: 1) reaction rates are limited by

459   the maximum specific uptake rate of succinate and are hence independent of its concentration (Beun et

460   al., 2000), 2) sufficient amount of buffer is added to the solution to keep the pH level constant, 3) three

461   nitrogen reductase enzymes ($\xi_{sat,NOR}$ for *NO* reduction, $\xi_{sat,NIR}$ for nitrite reduction and $\xi_{sat,NAP}$ for

462   nitrate reduction) can have saturation values varying between 0 (i.e. non-existing) and 1 in a bacterial cell,

463   and 4) inhibitory oxygen limits the reduction of *NO*, NO_2^- and NO_3^-. Reaction rates are designed to have a

464   dependency on the enzymes' level and biomass concentration with proper limiting/inhibiting terms.

465   Equation (12) is used to describe the evolution of each biochemical species. The final system of

466   advective-diffusive-reactive equations is adapted from (Kampschreur et al., 2012):

$$\frac{\partial C_i}{\partial t} + \nabla \cdot (C_i \boldsymbol{u}) = -\nabla \cdot \left(D_i \nabla C_i - D_i \frac{1 - H_i}{\alpha + (1 - \alpha)H_i} C_i \nabla \alpha \right) + R_i,$$
$$i = suc, O_2, NO_3^-,\ NO_2^-, NO, N_2O \qquad\qquad in\ \Omega_\vartheta \tag{28}$$

$$R_{suc} = -(r_{suc,O_2} + r_{suc,NAP} + r_{suc,NIR} + r_{suc,NOR})$$

$$R_{O_2} = -1.2 r_{suc,O_2}$$

$$R_{NO_3^-} = -3.23 r_{suc,NAP}$$

$$R_{NO_2^-} = 3.23 r_{suc,NAP} - 6.45 r_{suc,NIR}$$

$$R_{NO} = 6.45 r_{suc,NIR} - 6.45 r_{suc,NOR}$$

$$R_{N_2O} = 3.23 r_{suc,NOR}$$

$$r_{suc,O_2} = \mu_{max} C_{bio} \frac{C_{O_2}}{K_{O_2}\left(1 + \frac{C_{NO}}{K_{I,NO,O_2}}\right) + C_{O_2}}$$

$$r_{suc,NAP} = \mu_{max} C_{bio} \xi_{sat,NAP} \frac{C_{NO_3}}{K_{NO_3} + C_{NO_3}} \frac{K_{I,O_2,NAP}^{nNAP}}{K_{I,O_2,NAP}^{nNAP} + C_{O_2}^{nNAP}}$$

$$r_{suc,NIR} = \mu_{max} C_{bio} \xi_{sat,NIR} \frac{C_{NO_2}}{K_{NO_2} + C_{NO_2}} \frac{K_{I,O_2,NIR}^{nNIR}}{K_{I,O_2,NIR}^{nNIR} + C_{O_2}^{nNIR}}$$

$$r_{suc,NOR} = \mu_{max} C_{bio} \xi_{sat,NOR} \frac{C_{NO}^2}{\left[C_{NO}\left(1 + \frac{C_{NO}}{K_{I,NO}}\right) + K_{NO}\right]^2} \frac{K_{I,O_2,NOR}}{K_{I,O_2,NOR} + C_{O_2}}$$

$$\frac{d\xi_{sat,NAP}}{dt} = \nu_{m,NAP} \frac{C_{NO_3}}{K_{NO_3,NAP} + C_{NO_3}} \frac{K_{I,O_2,NAP}}{K_{I,O_2,NAP} + C_{O_2}} \left(1 - \xi_{sat,NAP}\right)$$

$$\frac{d\xi_{sat,NIR}}{dt} = \nu_{m,NIR} \frac{C_{NO_2}}{K_{NO_2,NIR} + C_{NO_2}} \left(1 - \xi_{sat,NIR}\right)$$

$$\frac{d\xi_{sat,NOR}}{dt} = \nu_{m,NOR} \frac{C_{NO}}{K_{NO,NOR} + C_{NO}} \left(1 - \xi_{sat,NOR}\right)$$

$$\frac{dC_{bio}}{dt} = 2.2 r_{suc,O_2} + 1.8\left(r_{suc,NAP} + r_{suc,NIR} + r_{suc,NOR}\right)$$

467 The full list of modelling parameters used for this study can be found in **Error! Reference source not**
468 **found.** (see Supplementary Information).

469 Reactive transport simulations were performed until a quasi-steady state was achieved. This was
470 characterized by all chemical species concentrations reaching a steady-state as determined by the
471 degradation activity of the given distribution of microorganisms. Since microbial growth takes place at
472 much larger time scales than the pore-scale transport processes no significant growth takes place during
473 the simulated time period. Simulation results show that the presence of air in this two-phase system
474 affects the distribution of biochemical species. Air, as the non-wetting phase, occupies the central part of
475 the pore space while the aqueous phase is expected to cover the corners and crevices (Figure 6, a). For

476 oxygen with $H_{O_2} = 31$ a higher concentration is observed in the air compared to that of the adjacent

477 aqueous phase (Figure 6, d). An analysis of how the volatility of a tracer compound may affect its

478 residence time in the porous medium is given in the Supplementary Information. Since the biomass is

479 only present on the grain surfaces (Figure 6, b), oxygen, nitrate and succinate deplete as the microbially-

480 mediated reactions only at these micro-locations. Fresh oxygen and nitrate thus need to diffuse from the

481 bulk (either from the aqueous phase or the air) to the reactive sites. The regions with high (i.e. not

482 degraded) succinate concentrations are compatible with low concentration regions of oxygen and nitrate,

483 i.e. the reactions are limited by the bioavailable oxygen and nitrate (Figure 6, b-e). Finally, all three

484 enzymes have an increased abundance in anaerobic regions with an active biomass (saturation map of

485 nitrate reductase enzyme is shown in Figure 6, e). While the saturation of nitrate reductase enzyme grows

486 linearly with time (until 0.25 s), the rate at which the nitrite and NO reductase enzymes ($\xi_{sat,NIR}$ and

487 $\xi_{sat,NOR}$ respectively) growth is rather slow for the very beginning of the simulation (until ~0.2 s), but it

488 surges exponentially afterward. A spatially integrated assessment of the degradation processes showed

489 that for the presented example 99% of the total succinate degradation is attributed to aerobic respiration

490 while a trivial amount is attributed to the three anaerobic processes (nitrate reduction, nitrite reduction and

491 NO reductions).

492 The presented results highlight the ability of the model to combine a high-resolution simulation of multi-

493 phase flow and transport processes with the simulation of complex biogeochemical processes. This allows

494 for a realistic simulation of the micro-scale distribution of reactive processes and for the derivation of an

495 accurate aggregated description of these processes.

496
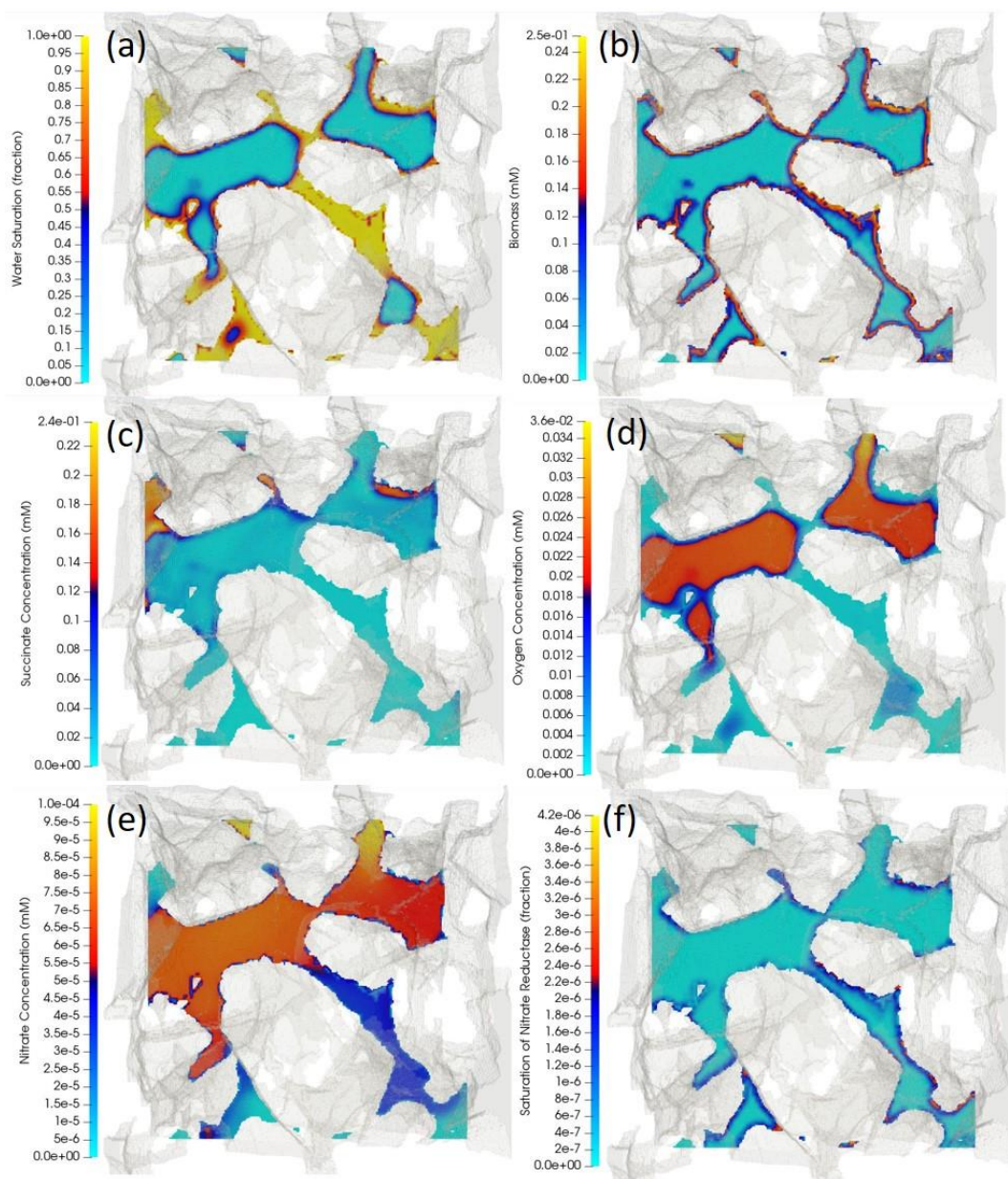
Figure 6: Cross-sectional view of the three dimensional porous medium. The opaque grayish background represents the 3D porous structure that is extracted and digitized from a μ-CT image. The colored surfaces are obtained by running a cutting plane through the middle of the sample and perpendicular to the z-axis. The distribution of (a) water saturation (i.e. water volume fraction), (b) biomass, (c) succinate, (d) oxygen, (e) nitrate and (f) nitrate reductase enzyme are respectively depicted with having yellow color indicating highest value and light blue as the lowest value. With air as the non-wetting phase, it is expected to fill in the middle of the pore space where capillary pressure is lower while water, as the wetting phase, is expected to occupy the corners (figure a). A high volatility constant for oxygen enforces to have higher concentrations of oxygen in the air compared to that of aqueous phase adjacent to the water-air interface.

505 As it can be seen from Figure 6, our model can be used (among other options) to identify clusters in

506 which succinate is most and least depleted. This would ease the process of analyzing the results by

507 isolating the parameters that are boosting/limiting the degradation of the carbon source. 3D visualization

508 of the oxygen and succinate distributions can be found in Golparvar et al. (2022).

509 **4.   Conclusion and future remarks**

510 In this paper, we have presented a newly developed modelling framework for simulating reactive

511 transport processes in real porous soil structures obtained from µ-CT images under unsaturated

512 conditions. The successful application of various benchmark test showed the model's accuracy in the

513 simulation of 1) the movement of water and air phase in variably saturated conditions via the enhanced

514 algebraic Volume of Fluid method (Raeini et al., 2012) coupled with the Navier Stokes equation, 2) the

515 transport of different species in both phases by the full advective-diffusive transport equation, and finally

516 3) using the operator splitting technique, an arbitrary set of biogeochemical reactions solved externally by

517 the Biogeochemical Reaction Network Simulator and communicated back into the main solver.

518 The presented model provides a novel and unique combination of pore-scale simulations of two-phase

519 flow, transport of dissolved and volatile species and their reactive transformations. This makes it an

520 accurate and powerful tool for the simulation of soil systems or other unsaturated porous media and of the

521 reactive transport processes therein. While developed with the aim for simulating biogeochemical

522 processes in soils the model is equally applicable for simulating other abiotic reactive processes coupled

523 to the dynamics of flow and transport in variably saturated pore structures of arbitrary geometry. Our

524 modelling framework is properly designed for simulating biogeochemical processes such as carbon-

525 nitrogen-sulfur-phosphorus cycles in soil as well as mixing and migration of contaminants in both

526 unsaturated soil and water aquifers. It comes with the benefit of explicit recognition of the soil structure,

527 phase dynamics/distributions and the capability of designing the complete redox reactions necessary for a

528 given process in a straightforward fashion. It is best suitable for running pre-pilot tests as feasibility

529 scenarios where the stakes for the success of the project are high. Also our model provides the best tool

530 for designing hypothetical experiments that are hard (if not impossible) to implement experimentally (e.g.

531 a specific distribution of biomass/reactants within the domain, or variation of specific properties of

532 reactive compound and/or the porous matrix). Furthermore, the high resolution modelling results

533 provided by this model support the upscaling of reactive-transport process description from the pore to

534 the continuum scale and from the process to the observation scale, respectively.

535 Although the current version of our numerical model is already covering a wide range of bio-physio-

536 chemical properties of the soil constituents, for having more realistic representation of multiphase,

multicomponent reactive transport in partially saturated porous media, few more factors still might be considered in future developments of the model: 1) shrinkage/expanding of the air/aqueous phase due to mass transfer of chemical species across fluid-fluid interface, 2) accounting for gas compressibility by adding an equation of state for tracking changes of air volume/density under flowing condition, 3) translating accumulated biomass on the grain surfaces into new flow-resistance components which would potentially change the velocity streamlines (i.e. bioclogging), 4) changes of the grain surface structures and of the associated solid-liquid interface due to mineral precipitation/dilution or due to accumulation/depletion of solid organic material and 5) chemotactic behavior of the microbial species.

5. Acknowledgements

This work was funded by the Helmholtz Association via the integrated project "Controlling Chemicals Fate."

6. Code and data availability

The source codes, benchmark and demonstration cases along with instruction for installing and running each case that are presented in this paper, are archived at https://github.com/amirgolp/P3D-BRNS_DOI: 10.5281/zenodo.6301317.

7. Author contributions

AR was responsible for model/software curation, validation and visualization. Conceptualization and methodology development were managed by AR, MK, and MT. Writing the original manuscript was handled by AR while all authors contributed to the revision and curation of the final draft. The entire work is supervised by MT.

8. Competing interests

The authors declare that they have no conflict of interest.

9. References

Aguilera, D. R., Jourabchi, P., Spiteri, C., and Regnier, P.: A knowledge-based reactive transport approach for the simulation of biogeochemical dynamics in Earth systems, Geochemistry Geophysics Geosystems, 6, Q07012, 10.1029/2004gc000899, 2005.
Albadawi, A., Donoghue, D. B., Robinson, A. J., Murray, D. B., and Delauré, Y. M. C.: Influence of surface tension implementation in Volume of Fluid and coupled Volume of Fluid with Level Set methods for bubble growth and detachment, International Journal of Multiphase Flow, 53, 11-28, https://doi.org/10.1016/j.ijmultiphaseflow.2013.01.005, 2013.

567 Baveye, P. C., Palfreyman, J., and Otten, W.: Research Efforts Involving Several Disciplines: Adherence
568 to a Clear Nomenclature Is Needed, Water Air Soil Poll, 225, ARTN 1997 10.1007/s11270-014-1997-7,
569 2014.
570 Baveye, P. C., Baveye, J., and John Gowdy, J.: Soil "Ecosystem" Services and Natural Capital: Critical
571 Appraisal of Research on Uncertain Ground., Frontiers in Environmetal Science, 4, 41,
572 10.3389/fenvs.2016.00041, 2016
573 Baveye, P. C., Otten, W., Kravchenko, A., Balseiro-Romero, M., Beckers, É., Chalhoub, M., Darnault,
574 C., Eickhorst, T., Garnier, P., and Hapca, S.: Emergent properties of microbial activity in heterogeneous
575 soil microenvironments: different research approaches are slowly converging, yet major challenges
576 remain, Frontiers in microbiology, 9, 1929, 2018.
577 Beun, J., Verhoef, E., Van Loosdrecht, M., and Heijnen, J.: Stoichiometry and kinetics of poly-β-
578 hydroxybutyrate metabolism under denitrifying conditions in activated sludge cultures, Biotechnology
579 and Bioengineering, 68, 496-507, 2000.
580 Bird, R. B.: Transport phenomena, Appl. Mech. Rev., 55, R1-R4, 2002.
581 Blunt, M. J.: Multiphase flow in permeable media: A pore-scale perspective, Cambridge University Press,
582 2017.
583 Brackbill, J. U., Kothe, D. B., and Zemach, C.: A continuum method for modeling surface tension, J
584 Comput Phys, 100, 335-354, https://doi.org/10.1016/0021-9991(92)90240-Y, 1992.
585 Centler, F., Shao, H., De Biase, C., Park, C.-H., Regnier, P., Kolditz, O., and Thullner, M.:
586 GeoSysBRNS-A flexible multidimensional reactive transport model for simulating biogeochemical
587 subsurface processes, Computers & Geosciences, 36, 397-405, 10.1016/j.cageo.2009.06.009, 2010.
588 Cirpka, O. A., and Valocchi, A. J.: Two-dimensional concentration distribution for mixing-controlled
589 bioreactive transport in steady state, Advances in Water Resources, 30, 1668-1679,
590 10.1016/j.advwatres.2006.05.022, 2007a.
591 Cirpka, O. A., and Valocchi, A. J.: Two-dimensional concentration distribution for mixing-controlled
592 bioreactive transport in steady state, Advances in Water Resources, 30, 1668-1679,
593 https://doi.org/10.1016/j.advwatres.2006.05.022, 2007b.
594 Cirpka, O. A., and Valocchi, A. J.: Reply to comments on "Two-dimensional concentration distribution
595 for mixing-controlled bioreactive transport in steady state" by H. Shao et al, Advances in Water
596 Resources, 32, 298-301, 10.1016/j.advwatres.2008.10.018, 2009.
597 Danckwerts, P. V., and Lannus, A.: Gas-liquid reactions, Journal of The Electrochemical Society, 117,
598 369C, 1970.
599 Gharasoo, M., Centler, F., Regnier, P., Harms, H., and Thullner, M.: A reactive transport modeling
600 approach to simulate biogeochemical processes in pore structures with pore-scale heterogeneities,
601 Environmental modelling & software, 30, 102-114, 2012.
602 Golparvar, A., Kästner, M., and Thullner, M.: Pore-scale modeling of microbial activity: What we have
603 and what we need, Vadose Zone Journal, 20, e20087, https://doi.org/10.1002/vzj2.20087, 2021.
604 Golparvar, A., Kaestner, M. and Thullner, M.: Movies, , doi:10.6084/m9.figshare.19391405.v2, 2022.
605 Graham, E., Grandy, S., and Thelen, M.: Manure effects on soil organisms and soil quality, Emerging
606 Issues in Animal Agriculture. Michigan State University Extension, 2014.
607 Graveleau, M., Soulaine, C., and Tchelepi, H. A.: Pore-Scale Simulation of Interphase Multicomponent
608 Mass Transfer for Subsurface Flow, Transport Porous Med, 120, 287-308, 10.1007/s11242-017-0921-1,
609 2017.
610 Greenshields, C. J.: OpenFOAM user guide, OpenFOAM Foundation Ltd, version, 3, 47, 2015.
611 Haroun, Y., Legendre, D., and Raynal, L.: Volume of fluid method for interfacial reactive mass transfer:
612 Application to stable liquid film, Chemical Engineering Science, 65, 2896-2909,
613 https://doi.org/10.1016/j.ces.2010.01.012, 2010.
614 Hirt, C. W., and Nichols, B. D.: Volume of fluid (VOF) method for the dynamics of free boundaries, J
615 Comput Phys, 39, 201-225, https://doi.org/10.1016/0021-9991(81)90145-5, 1981.
616 Issa, R. I.: Solution of the implicitly discretised fluid flow equations by operator-splitting, J Comput Phys,
617 62, 40-65, 1986.

618 Kampschreur, M. J., Kleerebezem, R., Picioreanu, C., Bakken, L. R., Bergaust, L., de Vries, S., Jetten, M.
619 S., and Van Loosdrecht, M.: Metabolic modeling of denitrification in Agrobacterium tumefaciens: a tool
620 to study inhibiting and activating compounds for the denitrification pathway, Frontiers in microbiology,
621 3, 370, 2012.
622 Kuzyakov, Y., and Blagodatskaya, E.: Microbial hotspots and hot moments in soil: Concept & review,
623 Soil Biology and Biochemistry, 83, 184-199, https://doi.org/10.1016/j.soilbio.2015.01.025, 2015.
624 Li, X. Y., Huang, H., and Meakin, P.: A three-dimensional level set simulation of coupled reactive
625 transport and precipitation/dissolution, Int J Heat Mass Tran, 53, 2908-2923,
626 10.1016/j.ijheatmasstransfer.2010.01.044, 2010.
627 Meakin, P., and Tartakovsky, A. M.: Modeling and simulation of pore-scale multiphase fluid flow and
628 reactive transport in fractured and porous media, Reviews of Geophysics, 47, 2009.
629 Meile, C., and Scheibe, T. D.: Reactive Transport Modeling of Microbial Dynamics, Elements, 15, 111-
630 116, 10.2138/gselements.15.2.111, 2019.
631 Nick, H. M., Raoof, A., Centler, F., Thullner, M., and Regnier, P.: Reactive dispersive contaminant
632 transport in coastal aquifers: numerical simulation of a reactive Henry problem, Journal of Contaminant
633 Hydrology, 145, 90-104, 10.1016/j.jconhyd.2012.12.005, 2013.
634 Parkhurst, D. L., and Appelo, C. A. J.: User's guide to PHREEQC (Version 2) : a computer program for
635 speciation, batch-reaction, one-dimensional transport, and inverse geochemical calculations, Report 99-
636 4259, 1999.
637 Patankar, S. V., and Spalding, D. B.: A calculation procedure for heat, mass and momentum transfer in
638 three-dimensional parabolic flows, Int J Heat Mass Tran, 15, 1787-1806, https://doi.org/10.1016/0017-
639 9310(72)90054-3, 1972.
640 Popinet, S.: An accurate adaptive solver for surface-tension-driven interfacial flows, J Comput Phys, 228,
641 5838-5866, https://doi.org/10.1016/j.jcp.2009.04.042, 2009.
642 Raeini, A. Q., Blunt, M. J., and Bijeljic, B.: Modelling two-phase flow in porous media at the pore scale
643 using the volume-of-fluid method, J Comput Phys, 231, 5653-5668, 2012.
644 Regnier, P., O'Kane, J. P., Steefel, C. I., and Vanderborght, J. P.: Modeling complex multi-component
645 reactive-transport systems: towards a simulation environment based on the concept of a Knowledge Base,
646 Applied Mathematical Modelling, 26, 913-927, https://doi.org/10.1016/S0307-904X(02)00047-1, 2002.
647 Sander, R.: Compilation of Henry's law constants (version 4.0) for water as solvent, Atmos. Chem. Phys.,
648 15, 4399-4981, 10.5194/acp-15-4399-2015, 2015.
649 Scardovelli, R., and Zaleski, S.: DIRECT NUMERICAL SIMULATION OF FREE-SURFACE AND
650 INTERFACIAL FLOW, Annual Review of Fluid Mechanics, 31, 567-603,
651 10.1146/annurev.fluid.31.1.567, 1999.
652 Schlüter, S., Zawallich, J., Vogel, H.-J., and Dörsch, P.: Physical constraints for respiration in microbial
653 hotspots in soil and their importance for denitrification, Biogeosciences Discussions, 1-31, 2019.
654 Schmidt, H., Vetterlein, D., Köhne, J. M., and Eickhorst, T.: Negligible effect of X-ray µ-CT scanning on
655 archaea and bacteria in an agricultural soil, Soil Biology and Biochemistry, 84, 21-27, 2015.
656 Steefel, C., and MacQuarrie, K.: Approaches to modeling of reactive transport in porous media, Reviews
657 in Mineralogy & Geochemistry, 34, 85-129, 1996.
658 Steefel, C. I., Appelo, C. A. J., Arora, B., Jacques, D., Kalbacher, T., Kolditz, O., Lagneau, V., Lichtner,
659 P. C., Mayer, K. U., Meeussen, J. C. L., Molins, S., Moulton, D., Shao, H., `imonek, J., Yabusaki, S. B.,
660 and Yeh, G. T.: Title Reactive transport codes for subsurface environmental simulation, 2015a,
661 Steefel, C. I., Appelo, C. A. J., Arora, B., Jacques, D., Kalbacher, T., Kolditz, O., Lagneau, V., Lichtner,
662 P. C., Mayer, K. U., Meeussen, J. C. L., Molins, S., Moulton, D., Shao, H., Šimůnek, J., Spycher, N.,
663 Yabusaki, S. B., and Yeh, G. T.: Reactive transport codes for subsurface environmental simulation,
664 Computational Geosciences, 19, 445-478, 10.1007/s10596-014-9443-x, 2015b.
665 Thullner, M., Van Cappellen, P., and Regnier, P.: Modeling the impact of microbial activity on redox
666 dynamics in porous media, Geochim Cosmochim Ac, 69, 5005-5019, 10.1016/j.gca.2005.04.026, 2005.

667 Thullner, M., Regnier, P., and Van Cappellen, P.: Modeling Microbially Induced Carbon Degradation in
668 Redox-Stratified Subsurface Environments: Concepts and Open Questions, Geomicrobiology Journal, 24,
669 139-155, 10.1080/01490450701459275, 2007.
670 Thullner, M.: Comparison of bioclogging effects in saturated porous media within one- and two-
671 dimensional flow systems, Ecological Engineering, 36, 176-196, 10.1016/j.ecoleng.2008.12.037, 2010.
672 Thullner, M., and Regnier, P.: Microbial Controls on the Biogeochemical Dynamics in the Subsurface,
673 Reviews in Mineralogy and Geochemistry, 85, 265-302, 10.2138/rmg.2019.85.9, 2019.
674 Tian, Z. W., and Wang, J. Y.: Lattice Boltzmann simulation of biofilm clogging and chemical oxygen
675 demand removal in porous media, Aiche J, 65, UNSP e16661 10.1002/aic.16661, 2019.
676 van Leer, B.: Towards the ultimate conservative difference scheme. V. A second-order sequel to
677 Godunov's method, J Comput Phys, 32, 101-136, https://doi.org/10.1016/0021-9991(79)90145-1, 1979.
678 Whitaker, S.: The method of volume averaging, Springer Science & Business Media, 2013.
679 White, A. F., and Brantley, S. L.: The effect of time on the weathering of silicate minerals: why do
680 weathering rates differ in the laboratory and field?, Chem Geol, 202, 479-506,
681 https://doi.org/10.1016/j.chemgeo.2003.03.001, 2003.
682 Yan, Z. F., Liu, C. X., Todd-Brown, K. E., Liu, Y. Y., Bond-Lamberty, B., and Bailey, V. L.: Pore-scale
683 investigation on the response of heterotrophic respiration to moisture conditions in heterogeneous soils,
684 Biogeochemistry, 131, 121-134, 10.1007/s10533-016-0270-0, 2016.
685